Outdoor mmWave Channel Modeling for Fixed Wireless Access at 60 GHz

Brecht De Beelde, Zeno Verboven, Emmeric Tanghe, David Plets, Wout Joseph

***Abstract*—The large bandwidths that are available at millimeter wave (mmWave) frequency bands allow high-throughput wireless communication systems that enable fixed wireless access (FWA) applications. In FWA networks, a stationary link is created between antennas installed at building facades or street furniture, such as lampposts. A Line-of-Sight (LOS) scenario is preferred, but to guarantee the quality of service to the user, communication should remain possible when the LOS path is obstructed. In this paper, outdoor channel models at 60 GHz are presented that can be used for the design and optimization of FWA networks, based on measurements with the Terragraph wireless system using IEEE Std. 802.11ad radios. LOS path loss (PL) measurement data is analyzed and building reflection loss, diffraction loss, and vegetation loss are measured. There is limited diffuse scattering, but reflections on the wall frame structure result in reflected paths with low losses. Existing vegetation models that are based on measurement campaigns at lower frequencies underestimate vegetation loss at mmWave frequencies, as measured excess attenuation values range from 15 to 25 dB for distances lower than 14 m. The presented channel models are used for link budget calculations for FWA networks.**

I. Introduction

According to the Shannon capacity theorem, the large bandwidths that are available in the millimeter wave (mmWave) frequency bands enable high-throughput wireless communication. Indoor applications include high-throughput access points for video streaming, gaming, and virtual and augmented reality (VR/AR), as well as wireless hubs and board-to-board interconnections in server rooms. Outdoors, cellular systems benefit from the increased bandwidth, e.g., in fifth-generation (5G) and future sixth-generation (6G) mobile networks. Another application for outdoor wireless communication at mmWave frequencies is fixed wireless access (FWA), in which fixed point-to-point wireless links provide internet connectivity to residential and enterprise buildings. FWA can be a cheaper alternative than deploying a fiber-optic network, as no digging is required and the infrastructure work is limited [1].

Reliable wireless channel models are critical for the design of wireless systems. Numerous indoor radio channel models at 60 GHz exist, and an overview of indoor mmWave channel models is provided in [2]. Indoor channel measurements at 60 GHz for wireless local area network (WLAN) applications are presented in [3], and the IEEE Std. 802.11ad wireless standard is designed for communication at 60 GHz, using channels with a bandwidth of 2.16 GHz [4]. In [5], good agreement is found between indoor measurements and ray-tracing simulations using geometrical optics and the uniform theory of diffraction. A statistical spatio-temporal model for large indoor environments shows that Line-of-Sight (LOS) paths and specular reflections are dominant over diffuse scattering [6]. Channel measurements at 60 GHz in an office environment are presented in [7]–[10]. A 60 GHz conference room channel model is provided in [11]. In [12], a train environment is considered, and channel models for a data center environment are presented in [13], [14]. In a hospital environment, lower path loss (PL) and delay spread values are found, compared to other indoor environments [15]. The influence of human activity on the 60 GHz indoor radio channel is discussed in [16], and a human blockage model is provided in [17], [18]. Indoor reflection and transmission measurements at various mmWave frequency bands are presented in [19]. Penetration loss measurements at 73 GHz are presented in [20]. Reflection and transmission measurements of interior structures of office buildings are presented in [21]. Penetration and reflection loss measurements at frequencies 60, 71, and 81 GHz are studied in [22]. The estimation of material characteristics at 60 GHz from power measurements is discussed in [23]. Throughput measurements for indoor scenarios using IEEE Std. 802.11ad transceivers are presented in [24]–[26], and network performance measurements, i.e., throughput and packet error rate (PER), are compared to a network performance prediction tool in [27] for a residential environment. The narrow beamwidth of the antenna systems used in actual 60 GHz communication systems results in a low angular spread, even for the metallic hull of a vessel [28], but reflections enable wireless communication in non-Line-of-Sight (NLOS) scenarios [29].

The number of outdoor channel models at mmWave frequencies is considerably lower, and most research considers channel models for 5G networks, i.e., at frequencies around 28-30 GHz [30], [31]. Outdoor channel models up to 18 GHz show that delay spread decreases and Ricean K-factor increases with frequency [32]. Similar to indoor environments, statistical outdoor radio channels at 60 GHz [33] show that a lower angular dispersion is observed. In [34], outdoor channel measurements are performed along a street canyon, with antennas mounted at a height of 3 m, and compared to ray-tracing simulations, confirming the channel sparsity. Ray-tracing requires accurate reflection and transmission properties. In [35], reflection and transmission measurements are performed at 60 GHz for a variety of building materials. Reflection on a brick and glass wall structure at E-band frequencies is discussed in [36].

In this work, we use the channel sounding platform that is presented in [37]. It consists of a customized pair of IEEE Std.

All authors are with Ghent University/IMEC, Department of Information Technology, Ghent, Belgium. E-mail:Brecht.DeBeelde@UGent.be

"An edited version of this paper was published by AGU. Published 2022 American Geophysical Union.:
De Beelde, B., Verboven, Z., Tanghe, E., Plets, D., & Joseph, W. (2022). Outdoor mmWave channel modeling for fixed wireless access at 60 GHz. Radio Science, 57, e2022RS007519. https://doi.org/10.1029/2022RS007519. "

802.11ad transceivers to measure double-directional angular PL, i.e., narrow-beam PL for different transmit and receive beams. This setup differs from traditional channel sounders that use antennas with a larger beamwidth and it allows for designing channel models that are representative of real network deployments. The same channel sounding platform is used to characterize the unmanned aerial vehicle (UAV) to ground wireless communication channel at 60 GHz, resulting in a PL model with quantification of beam misalignment [38]. Furthermore, the channel sounder is used for indoor PL and network performance measurements [27], [28] and outdoor measurements [34], [39]–[41].

The contributions of this paper are the following. (i) To the best of the authors' knowledge, this is the first time that outdoor building reflection and vegetation loss measurements near the tree trunk are performed at 60 GHz. (ii) A channel model for LOS and NLOS scenarios is presented that is based on measurements with a 60 GHz wireless communication system using IEEE Std. 802.11ad-compliant radios with narrow beamwidth antennas to be representative of real FWA network scenarios. (iii) Link budget considerations are discussed that take into account the LOS and NLOS channel models. These link budget calculations allow network dimensioning during the design of FWA networks.

The outline of this paper is as follows. In Section II, we first present the measurement equipment, followed by the different measurement scenarios. Section III contains the measurement results and channel models. Section IV present a discussion on link budget calculations using the presented channel models, and Section V concludes this paper.

II. Methodology

A. Measurement equipment

We use the IEEE Std. 802.11ad compliant Terragraph (TG) platform that is used in field trials for FWA network deployments [37]. Customized firmware allows using it as a channel sounding device, which is confirmed by validation measurements in an anechoic room.

1) Terragraph channel sounder: Each node of the TG sounder contains an array of 36 by 8 vertically polarized antenna elements with 0.55 λ interspacing. Independently controlled phase shifters on the horizontal antenna elements allow beamsteering in the azimuth plane, using pre-calibrated antenna weight vectors. The scanning range is -45° to 45°, with respect to the antenna's boresight, in steps of 1.4°. The maximum steering loss is 4.5 dB, i.e., the maximum gain of the antenna for the beams directed to ±45° is up to 4.5 dB lower than for the beam in the antenna's boresight direction. By selecting which antenna elements are active, the antenna array's beamwidth can be adjusted. For the measurements presented in this paper, a half-power beamwidth (HPBW) of 2.8° is used. This is the smallest possible HPBW of the TG sounder that is obtained by using all antenna elements, and this HPBW is representative of a realistic deployment of IEEE Std. 802.11ad wireless systems. The TG nodes are calibrated in a temperature-controlled environment over a range of ambient temperatures and gain settings. Transmitter calibration ensures an accurate equivalent isotropically received power (EIRP) reading for all gain settings and beam configurations, and the receiver calibration converts received signal strength information (RSSI) into incident power, considering the steering loss. The receiver calibration is valid for incident powers ranging from -90 dBm to -40 dBm. During the measurements, IEEE Std. 802.11ad waveforms are sent, and the measured received signal strength information (RSSI) and receiver gains are combined to get a power estimation. The operating frequency is 60.48 GHz, i.e., channel 2 of IEEE Std. 802.11ad, and the channel bandwidth is 2.16 GHz. PL is found by subtracting the calibrated RSSI from the EIRP and adding the receiver gain. A sequential beam sweep is performed, i.e., the measurement is repeated for all azimuth angles at both transmitter (TX) and receiver (RX), resulting in double-directional PL measurement results. The two nodes are connected to a control computer over a universal twisted pair (UTP) cable or via an out-of-band point-to-point wireless link in the 5 GHz industrial, scientific, and medical (ISM) frequency band. This connection is used for the coordination between the two nodes, e.g., to ensure that the beams of both TX and RX nodes are configured correctly and that they use the same IEEE Std. 802.11ad channel, and for gathering the measurement data.

2) Sounder validation in an anechoic room: The TG sounder is calibrated to convert power settings and antenna configurations to EIRP, and to convert RSSI and receiver gain settings to received power. In addition to the calibration, we have performed validation measurements in an anechoic room, with separations of 1 m and 2 m between the nodes. Figure 1 shows the validation for a distance of 2 m between the antennas, with an antenna beamwidth of 2.8°. The setup for the validation is presented in Fig. 1a, and Fig. 1b presents the measured PL angular profile (PLAP), showing PL as a function of angle of departure (AoD) and angle of arrival (AoA). The minimum PL is found for the AoD and AoA both equal to 0°. Sidelobes of the antenna array's radiation pattern result in a cross pattern in Fig. 1b, with an additional attenuation up to 25 dB compared to free space PL (FSPL) which is calculated via (1). In this equation, PL is the path loss in dB, d is the distance between the antennas in m, f is the frequency in Hz, and c is the speed of light in m/s.

$$\mathrm{PL}(d, f) = 20 \log_{10} \left(4\pi d \frac{f}{\mathrm{c}} \right) \tag{1}$$

For a distance of 1 m between the antennas, the minimum measured PL is 68.7 dB, compared to an FSPL of 68.0 dB. For a distance of 2 m, the minimum measured PL of 74.2 dB is slightly higher than the FSPL of 74.0 dB.

B. Measurement scenarios

Multiple scenarios are envisioned to characterize the 60 GHz outdoor radio channel for FWA communication systems. LOS PL is measured for antenna separations up to 130 m. For the characterization of NLOS channels, reflection loss is measured for different building facades, as well as diffraction loss. As the LOS path can also be blocked by vegetation, we performed vegetation loss measurements to characterize tree trunk attenuation at 60 GHz.

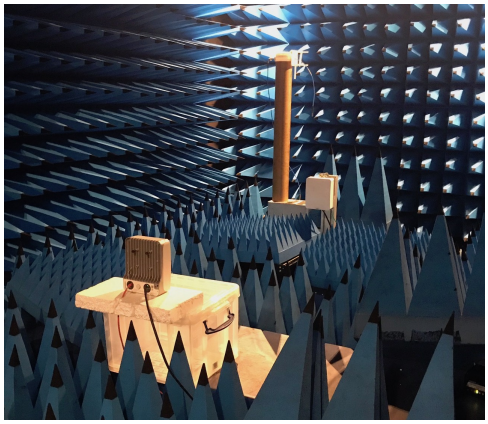

(a) Validation measurement setup

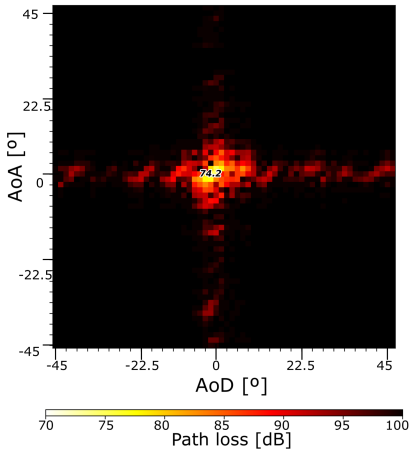

(b) Path loss angular profile (PLAP)

Figure 1. IEEE Std. 802.11ad Terragraph (TG) channel sounder validation in an anechoic room, with a distance of 2 m between the antennas.

1) Line-of-Sight path loss: The LOS measurements were performed along a road on a university campus. The TX node location was fixed, while the RX node was moved in steps of 10 m, with a minimum distance of 10 m and a maximum distance of 130 m between the two nodes. Both nodes were mounted on a tripod at a height of 1 m and were rotated by 90° to have the electric fields parallel with the ground and to perform scanning in the vertical plane, allowing to characterize ground-reflected paths.

The measured PL samples of the direct path, i.e., with AoD and AoA both equal to 0°, are compared to FSPL and fitted to the floating-intercept (FI) one-slope PL model from (2), with PL_0 the reference PL in dB at 1 m, n the dimensionless PL exponent, d the distance in meter, and χ a shadow fading term in dB, based on a normal distribution with zero mean and standard deviation σ [2].

$$\mathrm{PL}(d) = \mathrm{PL}_0 + 10\mathrm{n}\log_{10}(d) + \chi \tag{2}$$

2) Building reflection: In case the LOS link is blocked, NLOS links may allow wireless communication via a reflected path. To estimate the PL of the reflected paths, accurate reflection loss estimations are necessary. Therefore, building reflection loss measurements were performed for different incident angles and different types of building facades. The considered materials, shown in Fig. 2, are coated glass, fiber cement, and pebbled dash concrete. Specular reflection loss was measured for incident angles ranging from 0° to 60°, in steps of 15°, with respect to the building facade's normal. The nodes were positioned at a height of 1 m at a distance of 3 m from the reflection point. The incident angle is determined via geometry and a laser positioning system with mm-level accuracy is used to determine the distance to the wall and to the reflection point. The antennas were positioned with an accuracy of 1 cm, resulting in a maximum error of 1.5° of the incident angle. From the measurement results, reflection loss is obtained by subtracting FSPL for a distance of 6 m, i.e., 83.6 dB at 60.48 GHz, from the measured PL.

As buildings might contain different facade materials and intruding or protruding parts, we also performed reflection loss measurements for a concrete wall surrounded by protruding concrete parts, as can be seen in Fig. 2d. In this setup, the nodes were placed at a distance of 13 m from the facade, resulting in an incident angle of 22.5°. Furthermore, we performed reflection measurements on a glass window surrounded by concrete, with the two nodes positioned at a distance of 13 m from the window and with a spacing of 1.8 m, resulting in a small incident angle of 4°.

The relation between the incident and reflected electromagnetic fields is given by Fresnel's reflection coefficients that are based on the boundary conditions of electromagnetic fields [42]. The relation between the reflection coefficients, the incident and diffracted angles, and the refraction coefficients of the materials is presented in (3)-(4). In these equations, $r_\perp$ is the reflection coefficient for perpendicular polarization, i.e., the electric field is perpendicular to the plane of incidence, whereas, $r_\parallel$ is the coefficient for parallel polarization, i.e., the electric field is parallel to the plane of incidence. From the reflection coefficients that represent the ratio of incident and reflected field levels, the reflectance R, i.e., the ratio of reflected and incident power, is found by taking the square of the reflection coefficient (R = r^2).

$$r_\perp = \frac{n_i\cos(\theta_i) - n_t\cos(\theta_t)}{n_i\cos(\theta_i) + n_t\cos(\theta_t)} \tag{3}$$

$$r_\parallel = \frac{n_i\cos(\theta_t) - n_t\cos(\theta_i)}{n_i\cos(\theta_t) + n_t\cos(\theta_i)} \tag{4}$$

From the measured reflection loss, the reflection coefficient is obtained and used to estimate the refractive index of the different facades via a minimum mean squared error (MMSE) estimation of (5). In this equation, θ is the incident angle, n is the refractive index of the material under test (MUT) and r is the reflection coefficient for the perpendicular polarization. This equation follows from the Fresnel reflection coefficient (3) and Snell's law, using the trigonometric identity $\cos\theta = \pm\sqrt{1-\sin^2\theta}$, and $n_i = 1$.

$$r = \frac{\cos(\theta) - \sqrt{n^2 - \sin^2(\theta)}}{\cos(\theta) + \sqrt{n^2 - \sin^2(\theta)}} \tag{5}$$

(a) Coated glass

(b) Fiber cement

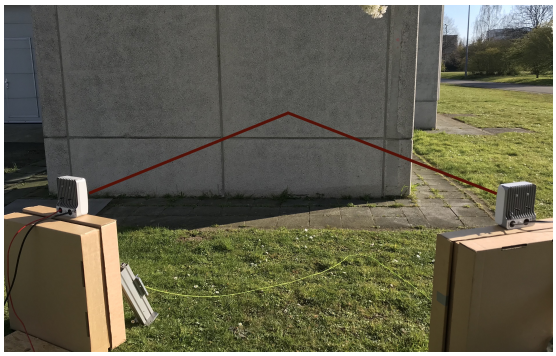

(c) Concrete

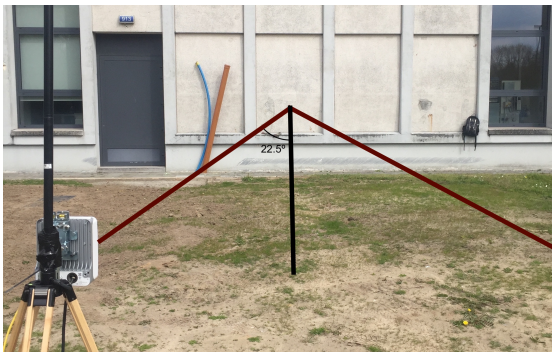

(d) Concrete with protruding parts

(e) Double-edge diffraction measurement setup for $\theta = 40°$ and $\phi = 35°$

Figure 2. Building reflection and diffraction loss measurement setups.

3) Double-edge diffraction: We measured diffraction around the double-edge concrete corner shown in Fig. 2e. Measurements were performed with two angles θ between the TX node and the wall, i.e., $\theta = 40°$ and $\theta = 45°$. The angle ϕ between the RX node and the wall ranges from 25° to 50° in steps of 5° for $\theta = 45°$. For $\theta = 40°$, measurements were performed with ϕ ranging from 35° to 45° in steps of 5°. Both antennas were positioned at a height of 1.5 m at a distance of 5 m from the corner. For the angles θ and ϕ, the distance to the wall is calculated via trigonometry which is used for the positioning of the two nodes. A measurement error of 2 cm in the distance measurement to the wall or the corner results in an angular error of a maximum of 0.6°. It can be seen in Fig. 2e that the corner has an indent of 0.44 m, resulting in double-edge diffraction.

The measured diffraction loss is compared to the knife-edge diffraction (KED) model [42].

4) Vegetation loss: We performed measurements in a planted forest with an average tree diameter of 10 cm. The different measurement scenarios are shown in Fig. 3. For each scenario, the nodes were placed at a height of 2.4 m, with antenna separations ranging from 2 m to 14 m. For the LOS measurements, the TX node location is fixed and an RX node location moves away from the TX node in steps of 2 m. The first Fresnel zone is never blocked by a tree. For the NLOS measurements, the TX node is behind a tree, and the RX node

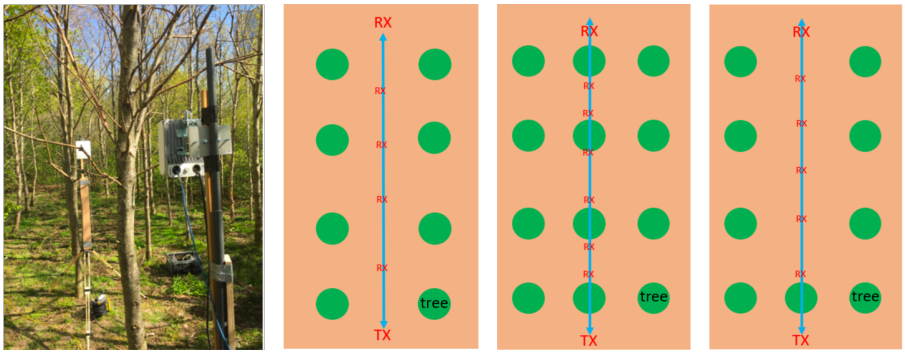

(a) Picture (b) LOS (c) NLOS (d) OBS

Figure 3. Vegetation loss measurement setups.

moves from tree to tree. Hence, with increasing distance, more trees are on the direct path between the antennas. As all trees are aligned on a grid, we can easily distinguish between LOS and NLOS scenarios. In the third scenario, i.e., obstructed LOS (OBS), the TX node is placed behind the tree, and the RX node moves away without any other tree obstructions.

III. Results

A. Line-of-Sight path loss

Figure 4 shows the measured PLAP for antenna separations 10 m and 80 m. Similarly to the validation measurement results presented in Sect. II-A2, a cross pattern is observed that is caused by the antenna radiation pattern. For distances up to 60 m, a ground reflection is observed. The sidelobes of the antenna system also cause a cross-pattern for this reflected path. At 10 m (Fig. 4a), the reflected component has an AoD and AoA of 11.3°, and a PL of 94.0 dB. As the beam angle of the reflected path is 1.4° for the distance of 80 m, which equals the beam spacing of 1.4° of the TX and RX beams, the reflected path cannot be distinguished from the LOS path (Fig. 4b).

Fitting all LOS PL samples of the direct path, with AoD and AoA equal to 0°, to the FI PL model from (2) results in a reference PL of 71.0 dB, a PL exponent of 1.78, and a standard deviation of 2.8 dB resulting in a 95% shadow margin of 3.5 dB. The reference PL is slightly higher than FSPL for a distance of 1 m, whereas the PL exponent is lower than the FSPL exponent of 2. For distances up to 60 m, the measured PL equals FSPL, calculated via (1), whereas measured PL is lower than FSPL for larger distances due to the presence of ground reflections.

The measured LOS PL is analyzed via the two-ray plane earth model [42]. For distances up to 60 m, the distance and incident angle of the ground-reflected path are calculated using the antenna height and antenna separation. The reflected path has a longer path length which causes a small additional FSPL, e.g., 0.2 dB for an antenna separation of 10 m. Subtracting the additional FSPL from the excess loss of the reflected path results in the reflection loss on the asphalt road. The reflection loss ranges from 4.2 dB for an antenna separation of 10 m (incident angle 78.7°) down to 1.0 dB for an antenna

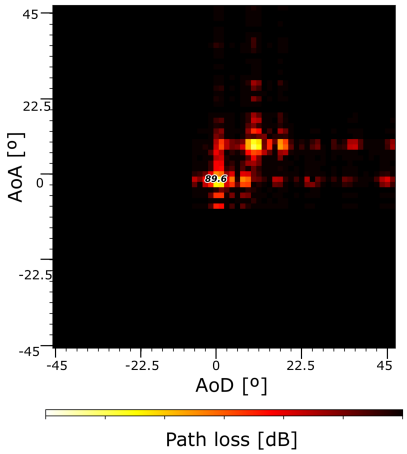

(a) Distance 10 m

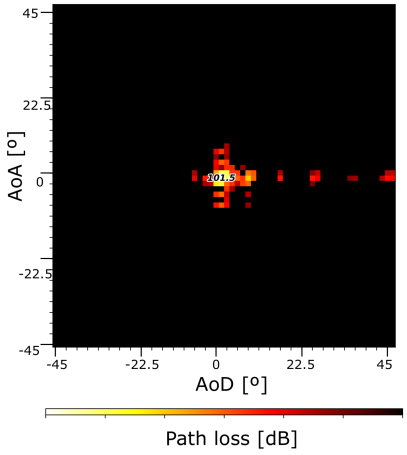

(b) Distance 80 m

Figure 4. PLAP of the LOS measurements for two antenna separations.

separation of 40 m (incident angle 87.1°). Estimating the refractive index of the road by an MMSE of the corresponding reflection coefficients to (5) results in n = 1.18. The total PL of the two-ray model can be calculated via (6), with c the speed of light, d the antenna separation in m, h the height of the TX and RX antennas in m, f the frequency in Hz, and R the reflection loss calculated via the reflection coefficient

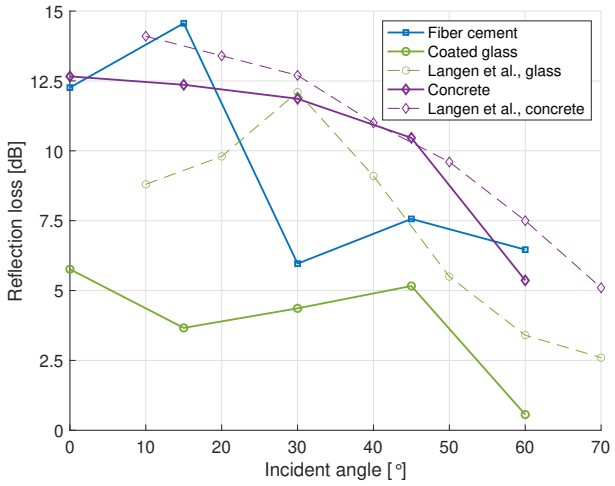

Figure 5. Reflection loss as a function of incident angle for different building facades, as well as measurement results by Langen et al.

obtained via (3), with n_i = 1 and n_t = 1.18.

$$\mathrm{PL}(d,f) = \left(\frac{\mathrm{c}}{4\pi df}\right)^2 \left|1 + \mathrm{R}e^{j\frac{2\pi f d}{\mathrm{c}}\left(2\sqrt{\left(\frac{d}{2}\right)^2+h^2}-d\right)}\right|^2 \quad (6)$$

The two-ray PL model from (6) predicts constructive interfering paths with a PL lower than FSPL for distances ranging from 70 m to 130 m. According to a two-ray plane earth PL model, it is expected that the PL exponent increases up to 4 only for distances exceeding $4\pi\frac{\mathrm{c}}{f}h^2$ which is 2.5 km for f = 60.48 GHz and with an antenna height h of 1 m.

The outdoor PL measurements presented in [40] show PL values that are 3 to 6 dB higher than FSPL, whereas our measurements show PL values equal to FSPL for lower distances and PL values lower than FSPL when the reflected path cannot be resolved in the PLAP. The RMSE between the measured PL samples and FSPL is 2.9 dB which is only slightly higher than the RMSE between the PL samples and the FI model. Therefore, we conclude that the free space PL model from (1) is a good model for FWA LOS links with highly directive antennas.

B. Reflection loss

Figure 5 shows the reflection loss as a function of incident angle for the different building facades. As expected, the reflection loss decreases for increasing incident angle, and the reflection loss of coated glass is up to 7 dB lower than concrete and fiber cement. The measured reflection loss of glass, with a thickness of 2 cm, is lower compared to the measurements at 60 GHz presented in [35], with glass of thickness 0.8 cm. This is caused by the coating and the presence of a security film with high permittivity, increasing the facade's reflectivity. The reflection loss is also lower than the (specular) reflection loss ranging from 5 dB for an incident angle of 70° to 11 dB for 10° [36]. The measured reflection loss of concrete is also up to 2 dB lower than [35]. Compared to measurements at 28 GHz, the measured losses are higher [43]. For glass, the reported reflection loss ranges from 3 to 4 dB for incident angles up to 60°. For concrete, the loss ranges from 5 to 6 dB. The measured reflection losses are much higher than the reflection loss of 1 to 4 dB for a brick wall, reported in [36].

The measured reflection coefficient of glass ranges from 0.52 for incident angle 0° up to 0.94 for angle 60°. It is higher than the reflection coefficient of tinted glass at 28 GHz [44]. A larger difference is found for the concrete wall, with reflection coefficients ranging from 0.54 for angle 0° down to 0.30 for angle 60°, compared to the reported reflection coefficient of 0.82 at 28 GHz for a concrete wall, given an incident angle of 10°.

An MMSE estimation of the refractive index results in n = 1.80 for fiber cement, n = 3.75 for glass, and n = 1.62 for concrete. The refractive index of glass is notably higher than the reported refractive index of 2.3 at 60 GHz [23] and 2.6 at 70 GHz [45] and the reported value of 2.25 at 140 GHz [46]. The refractive index of concrete corresponds to the reported value of 1.73 at 140 GHz [46]. The estimated refractive index values are lower than the values for drywall and plywood, based on the measurements from [36]. A higher reflection loss results in a lower refractive index.

Measurements with different angles with respect to the surface's normal of the TX and RX nodes reveal a limited effect of diffuse scattering but show that a reflected path can be found with low PL. This is illustrated in Fig. 6, for the fiber cement and glass facades, with an angle of 45° between the TX node and the facade's normal, and an angle of 0° between the RX node and the normal. Combining the measurement setup and TX and RX beam angles shows that the reflected paths correspond to a reflection on the wall structure that is indicated by the dashed rectangle in Fig. 2. This is also the case for the measurements from Fig. 2d. Reflection on the glass window with an incident angle of 4° results in a reflection loss of 6.2 dB, which is slightly higher than for the coated glass from Fig. 2a. The measurements and comparison to literature confirm that there is a large variation in reflection loss of glass windows, depending on the glass type [46]. Apart from the specular reflection, the PLAP also shows reflected paths with an additional loss, with a reflection on the metallic window frame. Specular reflection on the concrete part of the building results in a reflection loss of 13.5 dB for incident angle 22.5°. The presence of measurable reflections, even in non-specular scenarios, enables communication at 60 GHz even when the LOS path is blocked.

C. Double-edge diffraction

Figure 7 shows diffraction loss as a function of RX angle for two TX angles, as well as the calculated loss according to the KED model. No valid data is measured for the TX and RX angle combinations (θ=45°, ϕ=25°) and (θ=40°, ϕ=35°). As expected, the loss increases with increasing diffraction angle, i.e., decreasing RX angle considering a fixed TX angle. The KED model provides a good fit to the measured loss, with an RMSE between the model and measurements of 2.60 dB.

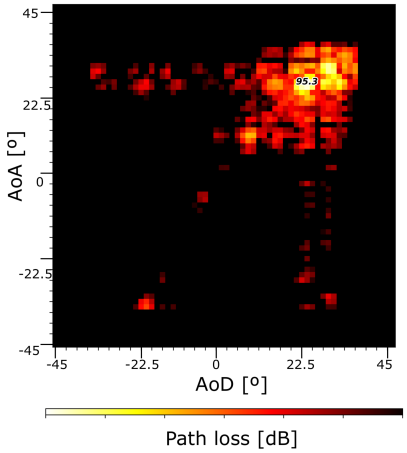

(a) Fiber cement facade

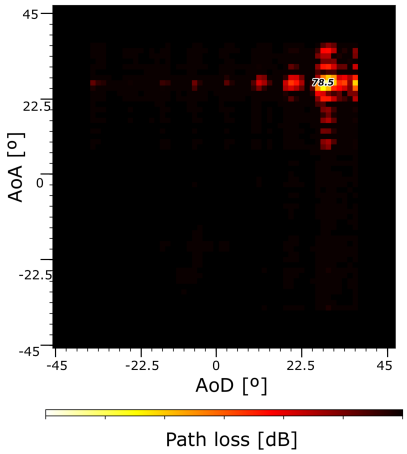

(b) Coated glass

Figure 6. PLAP of scattering measurements, with an angle of 45° between the TX node and the normal to the surface, and an angle of 0° between the RX node and the surface's normal.

D. Vegetation loss

Figure 8 shows the PLAP for the three measurement scenarios, i.e., LOS, OBS, and NLOS, for an antenna separation of 6 m. The LOS vegetation measurements show one main component at AoD and AoA equal to 0°, with PL values close to FSPL. Fitting the PL values of the direct path to the FI PL model from (2) results in a reference PL of 67.3 dB at 1 m, a PL exponent of 1.9, and a standard deviation of 1.6 dB. For the OBS and NLOS measurements, more reflections are present in the PLAP. For the OBS measurements, i.e., with one tree obstructing the direct path, the minimum PL is found for the diffracted path with AoD and AoA equal to 0°, whereas a reflected path with lower PL than the direct (obstructed) path exists for the NLOS measurements.

Figure 9 shows the measured PL for the three measurement scenarios from Fig. 3 as a function of distance. Fitting the NLOS PL values with the AoD and AoA equal to 0°, visualized by the green squares in Fig. 9, to the FI PL model from (2) results in a reference PL of 82.5 dB, a PL exponent of 3.4, and a standard deviation of 3.3 dB. The PL variations depend on the exact RX node location as follows. When the

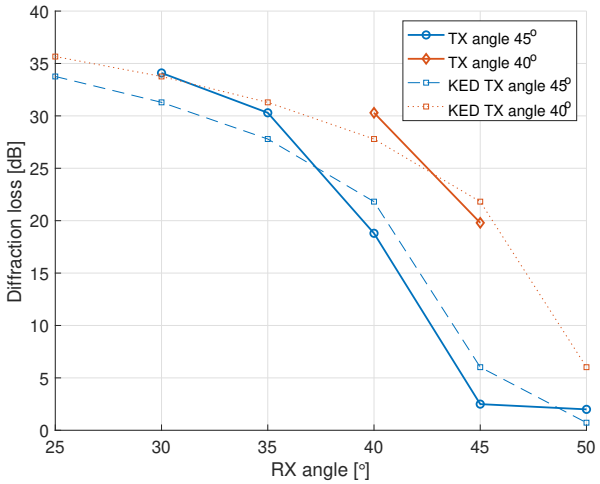

Figure 7. Diffraction loss as a function of RX angle, for TX angles 40° and 45°.

RX node is behind a tree, the PL is higher, whereas the PL gets lower when the distance from the RX node to the nearest tree is higher. The PL values of the best reflected path, represented by the yellow diamond symbols, are up to 7 dB lower than the PL of the direct (obstructed) path. These reflections have an AoD and AoA with opposite signs and are expected to correspond to paths path with a single tree reflection. For increasing distance, the ratio of the power of the obstructed LOS component to the power of the reflected components, i.e., with non-zero AoD and AoA, decreases. With only one tree in between the TX and RX nodes, visualized by the purple crosses in Fig. 9, the PL exponent is lower, as the diffraction angle decreases for longer distances, resulting in a lower diffraction loss. The excess loss when a single tree obstructs the LOS path ranges from 12 to 15 dB, which is higher than for sub-6 GHz frequencies, but lower than the tree trunk attenuation up to 25 dB at D-band frequencies [47].

In Fig. 9, we see that the excess loss, i.e., the difference between the measured NLOS PL and FSPL, ranges from 14 to 30 dB. The measured excess loss is high compared to well-known vegetation models for out-of-leaf scenarios. The Weissberger model from (7), with L the excess loss in dB, f the frequency in GHz, and d the distance in meter (limited to 14 m), predicts a loss ranging from 3.5 dB to 17.5 dB. The Weissberger model underestimates vegetation loss by up to 18 dB.

$$\mathrm{L} = 0.45 f^{0.284} d \tag{7}$$

The COST 235 vegetation model from (8), with L the excess loss in dB, f the frequency in MHz, and d the distance in meter, predicts an even lower loss ranging from 1.1 dB to 2.6 dB.

$$\mathrm{L} = 26.6 f^{-0.2} d^{0.5} \tag{8}$$

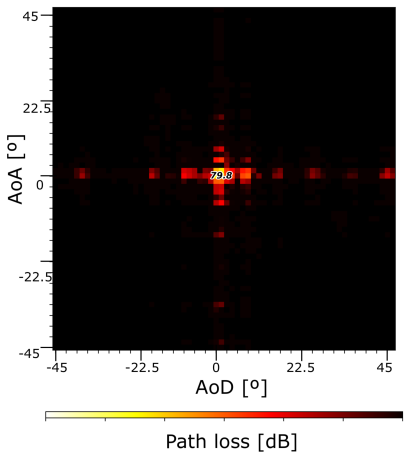

(a) LOS

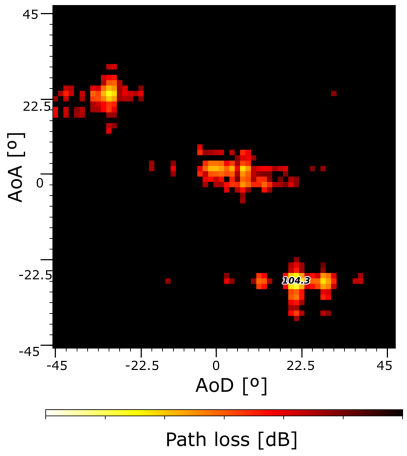

(b) NLOS

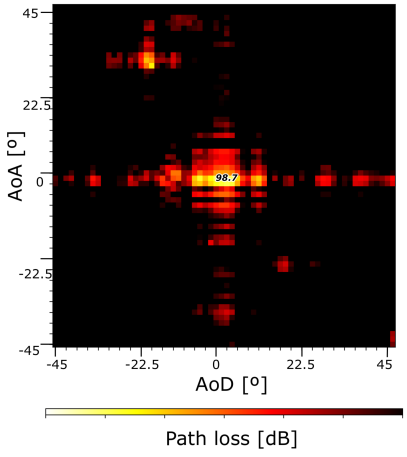

(c) OBS

Figure 8. PLAP for an antenna separation of 6 m for the three scenarios.

The FITU-R vegetation model from (9), with L the excess loss in dB, f the frequency in MHz, and d the distance in meter, estimates losses ranging from 14.4 dB to 39 dB.

$$\mathrm{L} = 0.37 f^{0.18} d^{0.59} \tag{9}$$

The measured excess loss is larger than the estimated loss from the Weissberger and COST 235 model because of the small antenna beamwidth. These models are fitted to measurements that are performed with antennas with a larger beamwidth. Larger-beamwidth antennas receive more incoherent components that are caused by scattering, which results in a higher received power and lower attenuation. For distances up to 9 m, the FITU-R model has a good fit to the measurement data, whereas, for larger distances, it overestimates the vegetation attenuation.

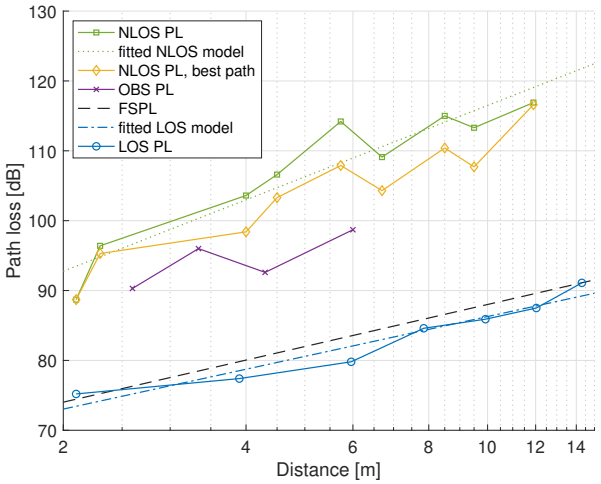

Figure 9. Path loss as a function of distance for three measurement scenarios: LOS with no trees between TX and RX nodes, OBS with a single tree between TX and RX, and NLOS with multiple trees between the TX and RX nodes.

Table I
LINK BUDGET PARAMETERS

Parameter	Value
Receiver sensitivity	-78 dBm to -53 dBm
Maximum throughput	27.5 Mbps to 4.620 Gbps
Transmit power	10.0 dBm
Total antenna gain	32.3 dBi
Feeding loss	2.5 dB
Implementation margin	4 dB

IV. LINK BUDGET CALCULATIONS FOR FWA NETWORKS

In this section, we use the channel modeling results to perform link budget calculations for FWA networks in the 60 GHz band. We consider IEEE Std. 802.11ad technology for which modulation schemes and corresponding receiver sensitivities and throughputs are provided in [4]. The link budget parameters are listed in Table I. A typical FWA node contains an antenna array of patch antennas. Considering a patch gain of 7.7 dBi [48] and an array of 36x8 elements (with a patch gain of 24.6 dB) results in a total antenna gain of 32.3 dBi. To apply to exposure regulations, the transmit power is considered to be 10 dBm [49]. Adding the TX antenna gain and subtracting a feeding loss of 2.5 dB results in a total effective isotropic radiated power (EIRP) of 39.8 dBm. We estimate received power using the models from Section III, by adding the antenna gain of the RX antenna to the EIRP and subtracting the feeding loss. An implementation margin

of 4 dB is added to account for system uncertainties. The maximum throughput that can be obtained depends on the received power and the receiver sensitivity. With a single carrier, a throughput up to 4.62 Gbps is possible using a square quadrature amplitude modulation (QAM) with 16 constellation points and a 3/4 code rate, i.e., modulation and coding scheme index 12 of the IEEE Std. 802.11ad specification.

In Fig. 10a, PL and throughput are presented as a function of distance for three scenarios: unobstructed LOS paths, NLOS paths with a single building reflection, and obstructed LOS paths with multiple trees in between the two antennas. For the LOS links, the maximum throughput of 4.6 Gbps can be obtained for distances up to 414 m. For the NLOS path, we use a reflection loss of 15 dB, which is the highest measured reflection loss in Section III-B, as a worst-case scenario. The maximum throughput can now only be obtained for distances up to 55 m, and no communication is possible for distances above 400 m. Due to the high vegetation loss, the throughput quickly drops in case multiple tree trunks are obstructing the LOS path.

During network design, it is important to determine the range that can be obtained for a certain throughput requirement. Therefore, we visualize the maximum link distance as a function of required throughput in Fig. 10b. While guaranteeing a throughput of 2 Gbps, LOS links up to 1.3 km are possible. When the link uses a building reflection, the maximum link distance decreases to 200 m. For two building reflections, the link distance further decreases to 30 m. The maximum link distance is 120 m for a single tree obstruction, and further decreases to 20 m for multiple trees in the path, e.g., in an avenue with trees on both sides of the road.

Using the average reflection loss of 10 dB, averaged over different incident angles and building facades, instead of the worst-case reflection loss of 15 dB results in a link distance of 440 m for the NLOS scenario with a single building reflection. It should also be noted that the NLOS vegetation scenario is a worst-case scenario. It is unlikely that all tree trunks are aligned with the direct path, or that trees are aligned along the full path. For links with trees that are partly obstructing the directed path over a distance of 10 m, an excess loss of 28 dB is added to a LOS model, and the maximum link distance to guarantee a throughput of 1 Gbps extends to 43 m.

In FWA deployments, a mesh network is considered where the user nodes connect to other user nodes, and data gets routed towards a point of presence which is the connection to the wired infrastructure. From the link budget calculation results, we conclude that a wireless mesh network deployment at 60 GHz will be able to bring high-throughput internet connectivity to the user. Even for an NLOS scenario with two building reflections, link distances of 50 m can be used for throughputs up to 770 Mbps, which is higher than most wired access networks that are used today. The aggregated data from multiple users can be combined and sent to another node using an NLOS link with a single reflection and a distance up to 180 m. Nodes close to the fiber point of presence will need a LOS link that has enough throughput to transfer the aggregated data. Planning of FWA networks will require knowledge of the environment, i.e., locations of buildings and vegetation, to optimize the network.

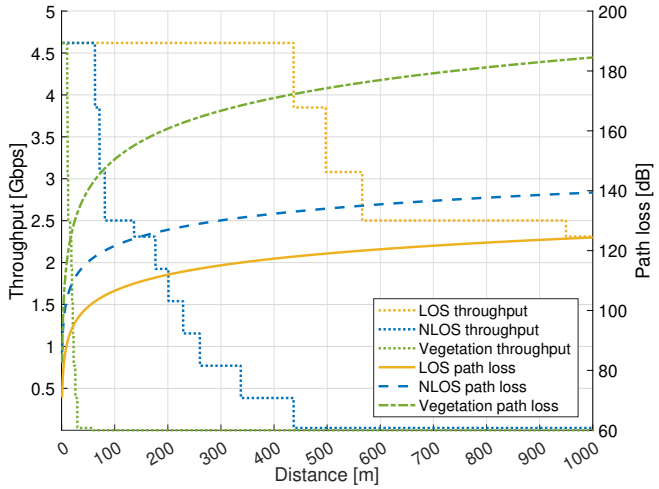

(a) Throughput as a function of distance

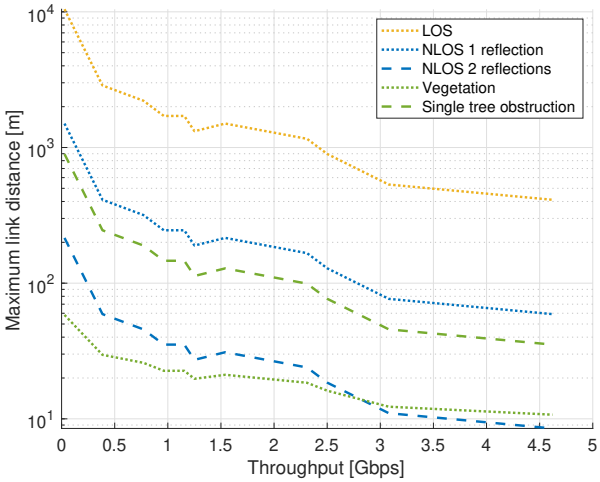

(b) Maximum link distance as a function of throughput

Figure 10. Throughput and range estimations via link budget calculations.

V. Conclusion

In this paper, we have investigated outdoor radio propagation characteristics at 60 GHz that are crucial for fixed wireless access applications. In the most favorable scenario, a LOS link exists and PL is close to free space PL. In case a LOS link does not exist, communication is possible via reflected paths, e.g., on nearby buildings. We discussed reflection loss measurements for different building facade materials and incident angles. The measured reflection loss is higher than at lower frequencies. Compared to literature on reflection loss at similar frequencies, the reflection loss of glass is up to 7 dB lower, because of a metallic film that is present in safety glass, whereas the reflection loss of concrete is similar. We performed vegetation loss measurements and showed that existing models that were developed based on measurements at lower frequencies and extrapolated to frequencies up to 100 GHz tend to underestimate actual tree attenuation at 60 GHz, due

to the narrow beamwidth of a realistic 60 GHz communication system. The FITU-R vegetation model provides the best fit to our measurement data. An additional loss up to 30 dB needs to be taken into account in a vegetated area. We also showed that a building corner causing double-edge diffraction can be modeled by a simple knife-edge diffraction model, which simplifies ray-tracing solutions for outdoor environments. Link budget considerations for FWA networks are analyzed, using the presented channel models. High-throughput LOS links with distances exceeding 1 km are possible, whereas the distance of NLOS links is limited to a few 100 m (via building reflection) or to a few 10 m (in an environment where tree trunks obstruct the direct path).

Future work includes network planning for the design of FWA networks, i.e., defining the locations of FWA edge nodes that are required to create a mesh network to connect all users. Furthermore, a routing algorithm will be designed to define how traffic is routed in the mesh network, taking into account the capacity of each wireless link, based on the link budget calculations presented in this paper.

ACKNOWLEDGMENT

This work was executed within the MM-WAVES research project, which is co-financed by IMEC and received support from Flanders Innovation & Entrepreneurship.

REFERENCES

[1] N. Ioannou, D. Katsianis, and D. Varoutas, "Comparative techno-economic evaluation of lte fixed wireless access, fttdp g.fast and fttc vdsl network deployment for providing 30 mbps broadband services in rural areas," *Telecommunications Policy*, vol. 44, no. 3, p. 101875, 2020. [Online]. Available: https://www.sciencedirect.com/science/article/pii/S0308596118303860

[2] A. Al-Saman, M. Cheffena, O. Elijah, Y. A. Al-Gumaei, S. K. Abdul Rahim, and T. Al-Hadhrami, "Survey of millimeter-wave propagation measurements and models in indoor environments," *Electronics*, vol. 10, no. 14, 2021. [Online]. Available: https://www.mdpi.com/2079-9292/10/14/1653

[3] N. Moraitis and P. Constantinou, "Indoor channel measurements and characterization at 60 ghz for wireless local area network applications," *IEEE Transactions on Antennas and Propagation*, vol. 52, no. 12, pp. 3180–3189, 2004.

[4] *IEEE 802.11ad*. IEEE Computer Society, 2012.

[5] A. Zhou, J. Huang, J. Sun, Q. Zhu, C. Wang, and Y. Yang, "60 ghz channel measurements and ray tracing modeling in an indoor environment," in *2017 9th International Conference on Wireless Communications and Signal Processing (WCSP)*, 2017, pp. 1–6.

[6] K. Haneda, J. Järveläinen, A. Karttunen, M. Kyrö, and J. Putkonen, "A statistical spatio-temporal radio channel model for large indoor environments at 60 and 70 ghz," *IEEE Transactions on Antennas and Propagation*, vol. 63, no. 6, pp. 2694–2704, 2015.

[7] A. Maltsev, R. Maslennikov, A. Sevastyanov, A. Khoryaev, and A. Lomayev, "Experimental investigations of 60 ghz wlan systems in office environment," *IEEE Journal on Selected Areas in Communications*, vol. 27, no. 8, pp. 1488–1499, 2009.

[8] D. Dupleich, F. Fuschini, R. Mueller, E. Vitucci, C. Schneider, V. Degli Esposti, and R. Thomä, "Directional characterization of the 60 ghz indoor-office channel," in *2014 XXXIth URSI General Assembly and Scientific Symposium (URSI GASS)*, 2014, pp. 1–4.

[9] Y. L. C. de Jong, J. A. Pugh, M. Bennai, and P. Bouchard, "2.4 to 61 GHz Multiband Double-Directional Propagation Measurements in Indoor Office Environments," *IEEE Transactions on Antennas and Propagation*, vol. 66, no. 9, pp. 4806–4820, SEP 2018.

[10] X. Wu, C. Wang, J. Sun, J. Huang, R. Feng, Y. Yang, and X. Ge, "60-ghz millimeter-wave channel measurements and modeling for indoor office environments," *IEEE Transactions on Antennas and Propagation*, vol. 65, no. 4, pp. 1912–1924, April 2017.

[11] A. Maltsev, R. Maslennikov, A. Sevastyanov, A. Lomayev, and A. Khoryaev, "Statistical channel model for 60 ghz wlan systems in conference room environment," in *Proceedings of the Fourth European Conference on Antennas and Propagation*, 2010, pp. 1–5.

[12] D. He, B. Ai, K. Guan, J. M. García-Loygorri, L. Tian, Z. Zhong, and A. Hrovat, "Influence of typical railway objects in a mmwave propagation channel," *IEEE Transactions on Vehicular Technology*, vol. 67, no. 4, pp. 2880–2892, 2018.

[13] M. Z. Zaaimia, R. Touhami, L. Talbi, M. Nedil, and M. C. E. Yagoub, "60-ghz statistical channel characterization for wireless data centers," *IEEE Antennas and Wireless Propagation Letters*, vol. 15, pp. 976–979, 2016.

[14] C. Gentile, P. B. Papazian, R. Sun, J. Senic, and J. Wang, "Quasi-deterministic channel model parameters for a data center at 60 ghz," *IEEE Antennas and Wireless Propagation Letters*, vol. 17, no. 5, pp. 808–812, 2018.

[15] M. Kyrö, K. Haneda, J. Simola, K. Nakai, K.-i. Takizawa, H. Hagiwara, and P. Vainikainen, "Measurement based path loss and delay spread modeling in hospital environments at 60 ghz," *IEEE Transactions on Wireless Communications*, vol. 10, no. 8, pp. 2423–2427, 2011.

[16] S. Collonge, G. Zaharia, and G. Zein, "Influence of the human activity on wide-band characteristics of the 60 ghz indoor radio channel," *IEEE Transactions on Wireless Communications*, vol. 3, no. 6, pp. 2396–2406, 2004.

[17] M. Jacob, S. Priebe, A. Maltsev, A. Lomayev, V. Erceg, and T. Kurner, "A ray tracing based stochastic human blockage model for the ieee 802.11ad 60 ghz channel model," *Proceedings of the 5th European Conference on Antennas and Propagation (EUCAP)*, pp. 3084–3088, 2011.

[18] M. Jacob, S. Priebe, T. Kürner, M. Peter, M. Wisotzki, R. Felbecker, and W. Keusgen, "Extension and validation of the ieee 802.11ad 60 ghz human blockage model," in *2013 7th European Conference on Antennas and Propagation (EuCAP)*, 2013, pp. 2806–2810.

[19] Y. Xing, O. Kanhere, S. Ju, and T. S. Rappaport, "Indoor wireless channel properties at millimeter wave and sub-terahertz frequencies," 2019. [Online]. Available: https://arxiv.org/abs/1908.09765

[20] J. Ryan, G. R. MacCartney, and T. S. Rappaport, "Indoor office wideband penetration loss measurements at 73 ghz," in *2017 IEEE International Conference on Communications Workshops (ICC Workshops)*, 2017, pp. 228–233.

[21] K. Sato, T. Manabe, T. Ihara, H. Saito, S. Ito, T. Tanaka, K. Sugai, N. Ohmi, Y. Murakami, M. Shibayama, Y. Konishi, and T. Kimura, "Measurements of reflection and transmission characteristics of interior structures of office building in the 60-ghz band," *IEEE Transactions on Antennas and Propagation*, vol. 45, no. 12, pp. 1783–1792, 1997.

[22] M. Khatun, C. Guo, and H. Mehrpouyan, "Penetration and reflection characteristics in millimeter-wave indoor channels," in *2021 IEEE-APS Topical Conference on Antennas and Propagation in Wireless Communications (APWC)*, 2021, pp. 1–5.

[23] L. Correia and P. Frances, "Estimation of materials characteristics from power measurements at 60 ghz," in *5th IEEE International Symposium on Personal, Indoor and Mobile Radio Communications, Wireless Networks - Catching the Mobile Future.*, vol. 2, 1994, pp. 510–513 vol.2.

[24] R. Nino, T. Nishio, and T. Murase, "Throughput measurement for ieee 802.11ad with various obstacles and reflectors by real machines," in *2021 IEEE 3rd Global Conference on Life Sciences and Technologies (LifeTech)*, 2021, pp. 401–402.

[25] T. Hirata and T. Murase, "Throughput measurement of ieee 802.11ad with various interferences on vehicles," in *2020 IEEE International Conference on Consumer Electronics - Taiwan (ICCE-Taiwan)*, 2020, pp. 1–2.

[26] S. K. Saha, A. Garg, and D. Koutsonikolas, "A first look at tcp performance in indoor ieee 802.11ad wlans," in *2015 IEEE Conference on Computer Communications Workshops (INFOCOM WKSHPS)*, 2015, pp. 63–64.

[27] B. De Beelde, A. Almarcha, D. Plets, and W. Joseph, "V-band channel modeling, throughput measurements, and coverage prediction for indoor residential environments," *Electronics*, vol. 11, no. 4, 2022. [Online]. Available: https://www.mdpi.com/2079-9292/11/4/659

[28] B. De Beelde, E. Tanghe, M. Yusuf, D. Plets, and W. Joseph, "Radio channel modeling in a ship hull: Path loss at 868 mhz and 2.4, 5.25, and 60 ghz," *IEEE Antennas and Wireless Propagation Letters*, vol. 20, no. 4, pp. 597–601, 2021.

[29] B. De Beelde, A. A. Lopéz, D. Plets, M. Yusuf, E. Tanghe, and W. Joseph, "Directive mmwave radio channel modeling in a ship hull," *International Journal of Microwave and Wireless Technologies*, p. 1–12, 2021.

[30] X. Zhao, S. Li, Q. Wang, M. Wang, S. Sun, and W. Hong, "Channel measurements, modeling, simulation and validation at 32 ghz in outdoor microcells for 5g radio systems," *IEEE Access*, vol. 5, pp. 1062–1072, 2017.

[31] S. K. M., S. A. Rao, and N. Kumar, "Modeling and link budget estimation of directional mmwave outdoor environment for 5g," in *2019 European Conference on Networks and Communications (EuCNC)*, 2019, pp. 106–111.

[32] V. Kristem, C. U. Bas, R. Wang, and A. F. Molisch, "Outdoor wideband channel measurements and modeling in the 3–18 ghz band," *IEEE Transactions on Wireless Communications*, vol. 17, no. 7, pp. 4620–4633, 2018.

[33] J. M. Kelner, C. Ziółkowski, and B. Uljasz, "Comparison of angular spread for 6 and 60 ghz based on 3gpp standard," in *2018 22nd International Microwave and Radar Conference (MIKON)*, 2018, pp. 286–290.

[34] M. Z. Aslam, Y. Corre, J. Belschner, G. S. Arockiaraj, and M. Jäger, "Analysis of 60-ghz in-street backhaul channel measurements and lidar ray-based simulations," in *2020 14th European Conference on Antennas and Propagation (EuCAP)*, 2020, pp. 1–5.

[35] B. Langen, G. Lober, and W. Herzig, "Reflection and transmission behaviour of building materials at 60 ghz," in *5th IEEE International Symposium on Personal, Indoor and Mobile Radio Communications, Wireless Networks - Catching the Mobile Future.*, vol. 2, 1994, pp. 505–509 vol.2.

[36] M. Kyrö, V. Semkin, and V.-M. Kolmonen, "Empirical characterization of scattering pattern of built surfaces at mm-wave frequencies," in *2013 7th European Conference on Antennas and Propagation (EuCAP)*, 2013, pp. 112–115.

[37] A. Shkel, A. Mehrabani, and J. Kusuma, "A configurable 60ghz phased array platform for multi-link mmwave channel characterization," in *2021 IEEE International Conference on Communications Workshops (ICC Workshops)*, 2021, pp. 1–6.

[38] S. Garcia Sanchez, S. Mohanti, D. Jaisinghani, and K. R. Chowdhury, "Millimeter-wave base stations in the sky: An experimental study of uav-to-ground communications," *IEEE Transactions on Mobile Computing*, pp. 1–1, 2020.

[39] M. H. Tariq, I. Chondroulis, P. Skartsilas, N. Babu, and C. B. Papadias, "mmwave massive mimo channel measurements for fixed wireless and smart city applications," in *2020 IEEE 31st Annual International Symposium on Personal, Indoor and Mobile Radio Communications*, 2020, pp. 1–6.

[40] K. Du, O. Mujumdar, O. Ozdemir, E. Ozturk, I. Guvenc, M. L. Sichitiu, H. Dai, and A. Bhuyan, "60 ghz outdoor propagation measurements and analysis using facebook terragraph radios," in *2022 IEEE Radio and Wireless Symposium (RWS)*, 2022, pp. 156–159.

[41] S. G. Sanchez and K. R. Chowdhury, "Robust 60ghz beamforming for uavs: Experimental analysis of hovering, blockage and beam selection," *IEEE Internet of Things Journal*, pp. 1–1, 2020.

[42] S. R. Saunders, *Antennas and Propagation for Wireless Communication Systems*, 1st ed. USA: John Wiley & Sons, Inc., 1999.

[43] K.-S. K. Byeong-Gon Choi, Won-Ho Jeong, "Characteristics analysis of reflection and transmission according to building materials in the millimeter wave band," *Recent Advances on Electroscience and Computers*, 2015.

[44] T. S. Rappaport, S. Sun, R. Mayzus, H. Zhao, Y. Azar, K. Wang, G. N. Wong, J. K. Schulz, M. Samimi, and F. Gutierrez, "Millimeter wave mobile communications for 5g cellular: It will work!" *IEEE Access*, vol. 1, pp. 335–349, 2013.

[45] R. Piesiewicz, T. Kleine-Ostmann, N. Krumbholz, D. Mittleman, M. Koch, and T. Kürner, "Terahertz characterisation of building materials," *Electronics Letters*, vol. 41, pp. 1002–1004(2), September 2005. [Online]. Available: https://digital-library.theiet.org/content/journals/10.1049/el_20052444

[46] B. De Beelde, D. Plets, C. Desset, E. Tanghe, A. Bourdoux, and W. Joseph, "Material characterization and radio channel modeling at d-band frequencies," *IEEE Access*, vol. 9, pp. 153 528–153 539, 2021.

[47] B. De Beelde, R. De Beelde, E. Tanghe, D. Plets, K. Verheyen, and W. Joseph, "Vegetation loss at d-band frequencies and new vegetation-dependent exponential decay model," *IEEE Transactions on Antennas and Propagation*, pp. 1–1, 2022.

[48] J. Zhan, J. Wen, L. Sun, and X. Shu, "Design of 60 ghz mm-wave patch antenna arrays," in *2015 IEEE 16th International Conference on Communication Technology (ICCT)*, 2015, pp. 262–265.

[49] P. F. M. Smulders, "Impact of regulations on feasible distance between 60 ghz devices," in *Proceedings of the Fourth European Conference on Antennas and Propagation*, 2010, pp. 1–4.